Magnetostructural coupling and multiferroic properties in the spin-frustrated system $Ni_{1-x}Zn_xCr_2O_4$

K. Devi Chandrasekhar,[1] J. Krishna Murthy,[2] J.-Y. Lin,[3] H. C. Wu,[1] W. J. Tseng,[1] A. Venimadhav,[4] and H. D. Yang[1,*]

[1]*Department of Physics and Center for Nanoscience and Nanotechnology, National Sun Yat-Sen University, Kaohsiung 804, Taiwan*

[2]*Department of Physics, Indian Institute of Science, Bangalore 560012, India*

[3]*Institute of Physics, National Chiao Tung University, Hsinchu 30010, Taiwan*

[4]*Cryogenic Engineering Centre, Indian Institute of Technology, Kharagpur 721302, India*

The magnetic phase diagram of $Ni_{1-x}Zn_xCr_2O_4$ demonstrates complex magnetic transitions for $x = 0.05$ with two long-range magnetic-order transitions at $T_{C1} = 41$ K and $T_{C2} = 17$ K. A glasslike feature emerges between T_{C1} and T_{C2} with the application of a direct current (dc) magnetic field in alternating current (ac) susceptibility measurements. Dielectric measurements show a change from the conventional dielectric to a quantum-paraelectric-like behavior without anomalies near the magnetic ordering temperature in the range $0.05 < x \leqslant 1$. The strong correlation among magnetic, dielectric, and ferroelectric properties near the structural relaxation temperatures 41 and 17 K confirms the emergence of multiferroic behavior in $Ni_{0.95}Zn_{0.05}Cr_2O_4$. A significant x-ray magnetic circular dichroism signal at the Ni site and ac susceptibility measurements indicate a spin-canting behavior between T_{C1} and T_{C2}. The dilute doping of the non-Jahn-Teller Zn ion in the Jahn-Teller Ni site modulate the different magnetic exchange interactions of Ni and Cr, which could invoke spin-canting and multiferroic behaviors.

I. INTRODUCTION

Frustration in a spin system can spawn unconventional and exotic magnetic phases [1,2]. An example of the simplest spin frustration is the antiferromagnetic (AFM) interaction in a triangular lattice, in which conflict arises between the geometry of the space inhabited by set of degrees of freedom and the local coordination favored by their interactions [1]. The intriguing complex coupling between the spin orientation constraints on lattice geometry results in a number of unusual magnetic ground states [2–7]. Often, if the strength of the frustration is weakly connected with the atomic lattice, unusual spin-disorder phases are formed, such as the spin-ice and spin-liquid behaviors [4–7]. However, if the spin frustration is firmly connected with the lattice, strong magnetoelastic coupling occurs; the appearance of magnetoelastic effects in which the spin is strongly coupled with the lattice degrees of freedom is an efficient approach to removing the ground state degeneracy in frustrated magnets [8,9]. In general, such a magnetoelastic effect in the frustrated lattice breaks the symmetry of the crystal via cooperative spin-lattice coupling [8].

Magnetoelastic effects have been widely examined in chromium spinel oxides [3,10]. Based on the A site, several fascinating magnetodielectric (MD) and multiferroic (MF) phases have been observed [11–15]. At high temperature, ACr_2O_4 stabilized in a normal cubic spinel structure with the space group $Fd\text{-}3m$. In the unit cell, A^{2+} ions form a diamond lattice with the tetrahedral oxygen (T_d) environment. The magnetic Cr^{3+} ions occupy the octahedral oxygen cage (O_h) and form a pyrochlore sublattice. In the local crystal field of oxygen ions, the $3d$ orbitals of a Cr^{3+} ion split into a low-lying t_{2g} triplet and a higher-energy doublet, for example, and Cr^{3+} stabilizes in the high-spin state ($S = 3/2$) [16]. According to the A-site cation, ACr_2O_4 systems are broadly classified into three categories. For nonmagnetic elements ($A =$ Zn, Cd, and Hg), the exchange interaction between the Cr^{3+} ($J_{Cr\text{-}Cr}$) ions in the pyrochlore lattice is highly frustrated; this frustration has been lifted by the symmetry-lowering spin-driven Jahn-Teller (SJT) distortion [9,16,17]. Spin frustration at the lattice imposes much lower magnetic ordering than expected and is usually defined by the term $f = |\theta_{CW}/T_N|$, where θ_{CW} and T_N are the Curie-Weiss (CW) and Néel temperatures, respectively [18]. SJT-accompanied lattice distortion changes the uniform magnetic exchange interaction between the Cr^{3+} pairs that leads to long-range AFM ordering. In $ZnCr_2O_4$, the frustration induces the magnetostructural transition observed at 12 K, where a change from the cubic to the tetragonal structure, along with the AFM ground state, has been experimental verified [9].

However, the presence of a magnetic element at the A site introduces an additional magnetic exchange interaction between the A and the B sites ($J_{A\text{-}Cr}$). In general, the strength of $J_{A\text{-}Cr}$ is larger than that of $J_{Cr\text{-}Cr}$; it overcomes the frustrated interaction between the Cr^{3+} ions in the pyrochlore lattice and prompts multiple magnetic orders [10,16]. Often, these systems exhibits weak magnetoelastic coupling; this has been verified by optical phonon-mode analysis in ACr_2O_4 systems, where a magnetic A site without orbital degeneracy remains in the cubic phase down to the lowest temperatures [8,10].

Second, if the A-site ion has orbital and spin degeneracy ($A =$ Fe, Ni, and Cu), additional complexity is introduced. The orbital Jahn-Teller (OJT) effect at the A site lowers the crystal symmetry from the cubic to the tetragonal space group $I4_1/amd$ even well above the magnetic ordering [19]. The strong spin-lattice coupling further reduces the lattice symmetry at the onset of the high-temperature ferrimagnetic (FIM) transition, indicating that the orbital degeneracy in the A site shows strong magnetoelastic coupling [19]. The annihilation of the Cr-site geometric spin frustration by the OJT effect has been observed at 310 K in $NiCr_2O_4$ [20]. Although geometric frustration is expected to vanish, the

---

*Corresponding author: yang@mail.nsysu.edu.tw

205143-1

resonancelike excitation observed in inelastic neutron diffraction measurements indicates that the *B*-site AFM ordered phase prevails over dynamic spin frustration, even in the OJT-active $NiCr_2O_4$ [21]. The spin structure of $NiCr_2O_4$ is composed of two sublattices, the FIM (longitudinal) and AFM (transverse) components [22]. For a magnetostructural coupling-driven tetragonal-to-orthorhombic transition, the longitudinal component of the Ni-Cr sublattice creates FIM long-range ordering at $T_C = 65$ K [13,19,22]. Further symmetry lowering of the orthorhombic structure occurs at $T = 30$ K. All these anomalies have been observed in magnetic and heat-capacity measurements [13,19]. In neutron diffraction, the Cr sublattice shows AFM ordering at this transition temperature [22]. The magnetic propagation vectors of the FIM (longitudinal) and AFM (transverse) components have been assigned to $\mathbf{k}_1 = 0$ and $\mathbf{k}_2 = (0,0,1)$, respectively [22].

Similar to chromates, magnetoelectric behavior has been verified in ferrites and vanadate systems [23,24]. However, in chromates, the MF behavior is strongly correlated with the crystal lattice via the spin-lattice coupling [10]. The present paper focuses on understanding the complex interplay of SJT and OJT and its rich phase diagram in a solid solution of the $Ni_{1-x}Zn_xCr_2O_4$ series. The spin frustration at the *B* site and orbital degeneracy of the *A* site modulate the magnetostructural transitions and MF properties of $Ni_{1-x}Zn_xCr_2O_4$.

II. EXPERIMENTAL DETAILS

The samples of the $Ni_{1-x}Zn_xCr_2O_4$ series were prepared by the solid-state reaction method. Stoichiometric precursor powders of NiO (>99%, Sigma-Aldrich), ZnO (>99%, Sigma-Aldrich), and Cr_2O_3 (>99%, Sigma-Aldrich) were ground thoroughly and pressed into pellets. The pellets were initially heat-treated at 800 °C for 12 h and then cooled slowly to room temperature. The final heat treatment of the pellets was performed at 1100 °C for 24 h after several intermediate regrinding processes. The quality and crystal structure of the $Ni_{1-x}Zn_xCr_2O_4$ samples were determined using high-resolution synchrotron x-ray diffraction (SXRD) at the 01C2-SWLS beamline of the National Synchrotron Radiation Research Center (NSRRC), Taiwan. A closed-cycle cryostat was used to control the temperature during the measurements. The samples were mounted on a glass tube, and data were collected in reflection geometry using a wavelength of $\lambda = 0.77941$ Å from 2° to 45° in 2θ. Rietveld refinement was performed using Fullprof suite software. Alternating current (ac) and direct current (dc) magnetic measurements were conducted using a Quantum Design Magnetic Property Measurement System (MPMS) system. X-ray magnetic circular dichroism (XMCD) measurements of the Ni *L* edge were performed at the Dragon beamline of NSRRC. A NiO single crystal was used for calibration. Measurements were conducted in the fluorescence yield (FY) mode at 27 K in a magnetic field of 1 T with circularly polarized light. For transport measurements (pyro and dielectric), both sides of the pellet were coated with conducting silver epoxy to enable electrical measurements. Dielectric and MD measurements were conducted using the Agilent 4294A impedance analyzer in conjunction with the Quantum Design Physical Property Measurement System (PPMS) system. The sample was placed as close to the bottom
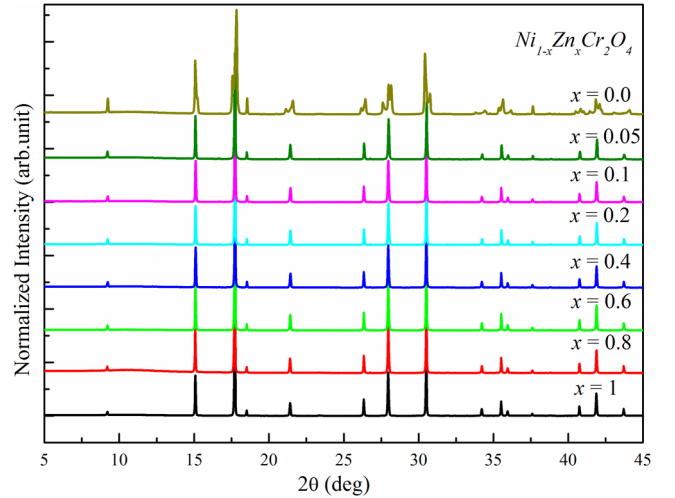

FIG. 1. Room temperature SXRD patterns of $Ni_{1-x}Zn_xCr_2O_4$ ($0 \leqslant x \leqslant 1$) series.

of the chamber as possible to ensure accurate temperature readings. Pyrocurrent measurements were acquired using the Keithley 6517B electrometer. During the measurement, the sample was cooled under the application of 700 V.

III. RESULTS AND ANALYSIS

A. Synchrotron x-ray diffraction

Room-temperature SXRD studies were performed to examine the purity and the crystal structure of the $Ni_{1-x}Zn_xCr_2O_4$ samples. From Fig. 1, the SXRD pattern of $NiCr_2O_4$ reveals a tetragonal crystal structure with the space group $I4_1/amd$, and the obtained lattice parameters $a = b = 5.824$ Å and $c = 8.85$ Å are consistent with those reported in the literature [20]. The tetragonal phase appears because of the presence of the Jahn-Teller (JT)-active Ni^{2+} ion at the *A* site of ACr_2O_4 systems [20]. However, dilution of the JT ion with a small concentration of a non-JT ion (Zn^{2+}) might stabilize the high-symmetry cubic crystal structure. As expected, the cubic lattice constant for $Ni_{1-x}Zn_xCr_2O_4$ ($x \geqslant 0.05$) increases with x in accordance with the ion radii of Zn (0.6 Å) and Ni (0.55 Å) (shown in Supplemental Material [25]). In the present paper, we observed that the formation of the cubic crystal structure began with 5% Zn^{2+} doping at the Ni^{2+} site. This clearly indicates that the morphotropic phase transition between the tetragonal and the cubic phase appears for a Zn concentration between 0 and 0.05.

B. Magnetic properties

The temperature-dependent zero-field cooling (ZFC) and field-cool cooling (FCC) magnetic susceptibility curves for the $Ni_{1-x}Zn_xCr_2O_4$ series are shown in Fig. 2(a). As reported, the χ-T data for the end members of $Ni_{1-x}Zn_xCr_2O_4$ ($x = 0$ and 1) are consistent with the reported literature [13,26]. The AFM ordering (T_N) at 13.2 K in $ZnCr_2O_4$ is attributed to the SJT distortion, in which spin frustration at the Cr^{3+} (d^3) pyrochlore lattice is lifted by the magnetostructural transition from the paramagnetic (PM) cubic phase to the AFM tetragonal phase
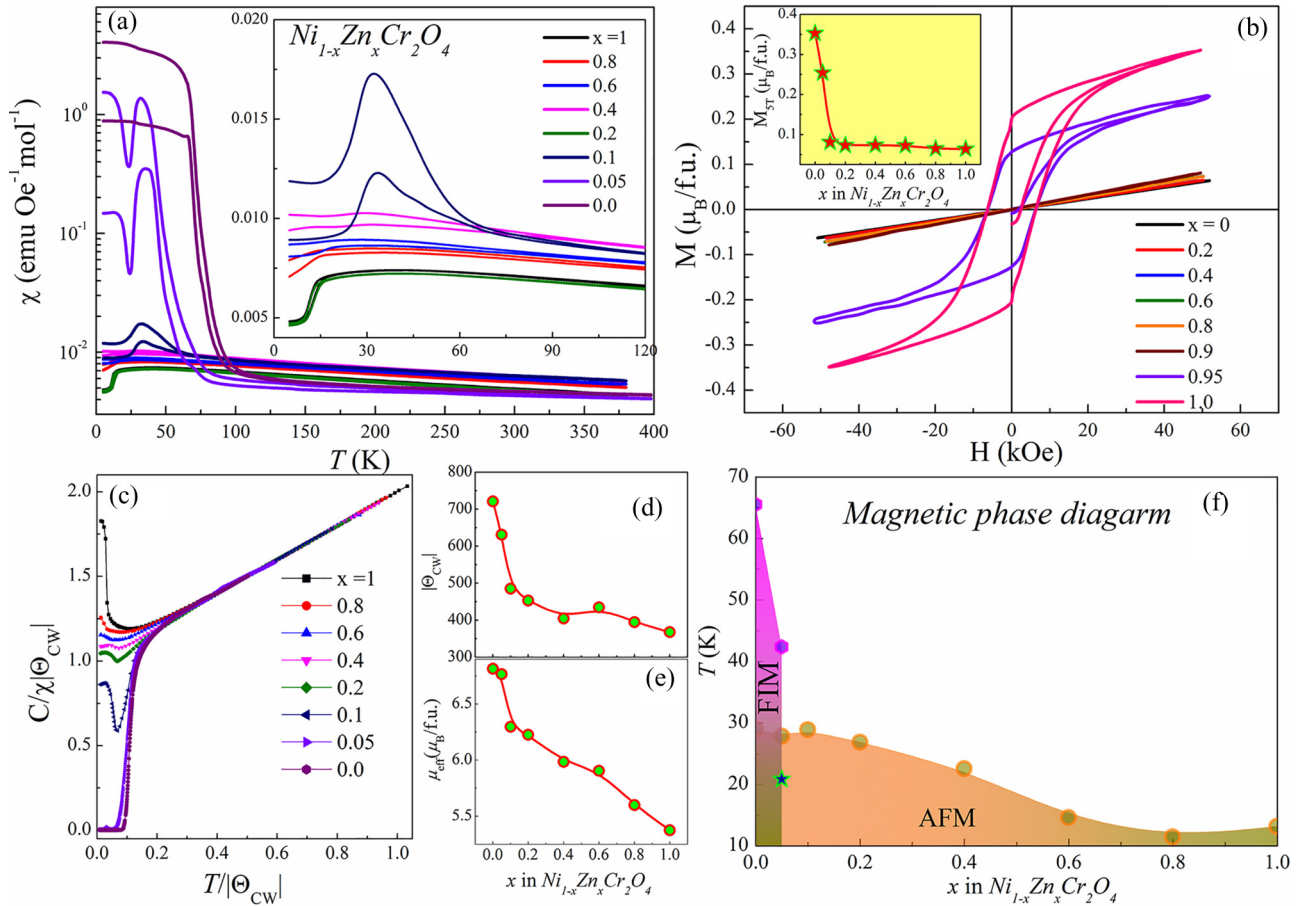
FIG. 2. (a) ZFC-FCW χ-T curves for Ni$_{1-x}$Zn$_x$Cr$_2$O$_4$; inset shows the magnified view. (b) M-H curves at 5 K; inset illustrates the variation of M_{5T} vs x in Ni$_{1-x}$Zn$_x$Cr$_2$O$_4$. (c) $\frac{C}{\chi|\Theta_{CW}|}$ vs $\frac{T}{|\Theta_{CW}|}$ plots for Ni$_{1-x}$Zn$_x$Cr$_2$O$_4$. (d) and (e) Variation of dielectric Θ_{CW} and μ_{eff} for x in Ni$_{1-x}$Zn$_x$Cr$_2$O$_4$. (f) Magnetic phase diagram of the Ni$_{1-x}$Zn$_x$Cr$_2$O$_4$ series.

with a spin-Peierls-like phase transition [27]. In the case of NiCr$_2$O$_4$, the FIM alignment of the Ni-Cr atom is set at 68 K(T_{C1}) and is accompanied by a structural change to orthorhombic symmetry that relieves the frustration [13]. The superimposed AFM Cr moments at 28 K(T_{C2}) show a second magnetic transition that results in a noncollinear magnetic structure [13,19,22]. For the intermediate compounds, the SJT-driven magnetic transition is progressively enhanced up to $x > 0.05$. However, for the $x = 0.05$ compound, the ZFC-FCCχ-T curves show complex multiple magnetic transitions with the decrease of temperature namely, a PM-to-FIM transition at $T_C = 41$ K, followed by an abrupt drop of the magnetization at 28 K. Further enhancement of the magnetization is observed below 20 K. The complete magnetic phase diagram is shown in Fig. 2(d). As shown in the figure, the magnetic ground state is more complex for $x = 0.05$ than for the NiCr$_2$O$_4$ sample. The magnetization vs field (M-H) curves for Ni$_{1-x}$Zn$_x$Cr$_2$O$_4$ at 5 K are shown in Fig. 2(b). The appearance of comparable hysteresis and a quantitatively similar loop shape for $x = 0.05$ confirm the FIM nature of the sample. However, the linear behavior of the M-H curves for $x > 0.05$ indicates strong AFM behavior. The magnetization at 5 T(M_{5T}) vs x at 5 K, shown in the inset of Fig. 2(b), clearly exhibits a sharp drop at $x > 0.05$; thereafter, M_{5T} is saturated.

We estimated the effective PM moment $\mu_{eff} = \sqrt{3K_B c/N_A}$, by fitting the CW equation $\chi = \frac{C}{T - \Theta_{CW}}$ well above the PM transition, where C and K_B are the Curie and Boltzmann constants, respectively. The parameters μ_{eff} and Θ obtained from the CW fits are shown Figs. 2(d) and 2(e). The μ_{eff} (5.37μ_B/formula unit, or f.u.) for ZnCr$_2$O$_4$ is consistent with the spin-only magnetic moment of Cr^{3+} ($S = 3/2$; $\mu_s = g\sqrt{S(S+1)}$) [26]. In the case of NiCr$_2$O$_4$, the obtained $\mu_{eff} = 6.84\mu_B$/f.u. is higher than the spin-only magnetic moment (6.16μ_B/f.u.). However, the present value is almost close to the total angular magnetic moment (7.1647μ_B/f.u.) for NiCr$_2$O$_4$, indicating partially unquenched orbital magnetic moment contribution for Ni^{2+} with $g_J = 5/4$ [19]. By varying the doping, μ_{eff} drops near $x = 0.05$; thereafter, a linear decrease trend is observed up to $x = 1$. In addition, Θ shows a similar variation to that of μ_{eff}.

For frustrated magnetic systems, the scaled CW plot ($\frac{C}{\chi|\Theta|} = \frac{T}{|\Theta|} + 1$) is often employed to effectively determine the magnetic correlation above T_C and to assess the validity of the CW fit in the PM region [26]. The normalized plots between $\frac{C}{\chi|\Theta_{CW}|}$ and $\frac{T}{|\Theta_{CW}|}$ for different x values are shown in Fig. 2(c). In the PM region, the scaling plots collapse into a single master curve, with a slope of 1, and intersect the y axis at 1, which indicates that the CW fits are satisfactory. For ZnCr$_2$O$_4$, an upturn of the scaling curve is observed
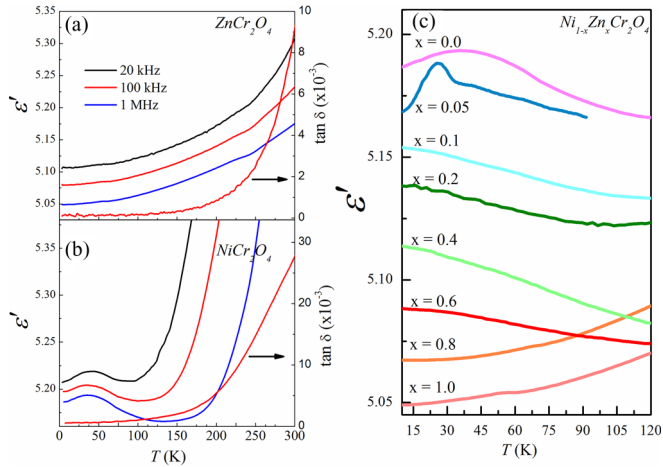
FIG. 3. Variation of dielectric permittivity vs T for (a) NiCr$_2$O$_4$ and (b) ZnCr$_2$O$_4$ with different frequencies. (c) Temperature-dependent dielectric permittivity of the Ni$_{1-x}$Zn$_x$Cr$_2$O$_4$ series for 1 MHz.

at $\frac{T}{|\Theta_{CW}|} \sim 0.033$; this value is lower than the frustrated limit ($\frac{T}{|\Theta_{CW}|} = 0.1$), indicating the highly frustrated nature of the system [26]. With an increasing Ni^{2+} concentration, this upturn progressively decreases, whereas $\frac{T}{|\Theta_{CW}|}$ shows an increasing trend, indicating that the A-site disorder in ACr$_2$O$_4$ destabilizes the spin frustration. This might be due to the complex magnetic interaction between the A-Cr ions. For $x = 0.05$ and NiCr$_2$O$_4$, the scaling curve shows a negative deviation that indicates FIM correlations.

C. Dielectric properties

The temperature-dependent dielectric properties for the end members of the series are shown in Figs. 3(a) and 3(b) at different frequencies. The dielectric permittivity of ZnCr$_2$O$_4$ smoothly varies with decreasing temperature, without showing any anomaly near the SJT ordering. A weak anomaly appeared only in $d\varepsilon'/dT$ near T_N (not shown). However, the dielectric permittivity demonstrates a peak near the FIM ordering in NiCr$_2$O$_4$; this suggests a close connection between the magnetic and the dielectric properties. In both cases, the observed dielectric permittivity (~ 5.05) and loss tangent ($\sim 10^{-3}$) values are extremely low and show a nondispersive behavior on the applied frequencies, which excludes the extrinsic parasitic contribution to the observed dielectric variations.

The temperature-dependent dielectric measurement results for the Ni$_{1-x}$Zn$_x$Cr$_2$O$_4$ series at the applied frequency of 1 MHz are displayed in Fig. 3(c). For the ZnCr$_2$O$_4$ system, $d\varepsilon'/dT$ shows a positive slope. However, this behavior is reversed for $x < 0.8$. The negative slope of $d\varepsilon'/dT$ in the composition range $0.1 > x > 0.6$ resembles that of quantum-paraelectric behavior [28]. The disorder at the A site in ACr$_2$O$_4$ might be the source of the observed transition from conventional dielectric to quantum-paraelectric-like behavior. Despite the change to quantum-paraelectric-like behavior, the dielectric property does not exhibit any anomaly near the magnetic ordering in the composition range $0.05 < x \leqslant 1$. However, for the $x = 0.05$ sample, $d\varepsilon'/dT$ shows a negative
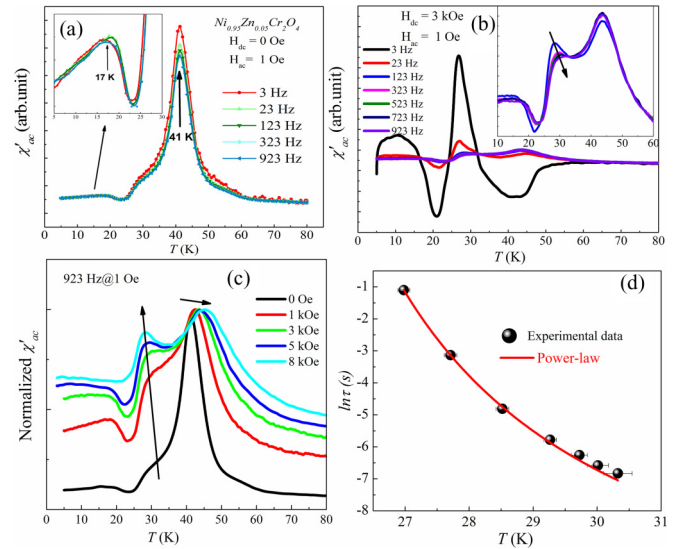

FIG. 4. (a) χ'_{ac} vs T for different frequencies; inset shows the magnified view of χ'_{ac} vs T curves at low temperature. (b) χ'_{ac} vs T under the dc field of 3 kOe; inset shows the magnified view of χ'_{ac} vs T curves at low temperature. (c) χ'_{ac} vs T for various dc fields. (d) $\ln\tau$ vs T curves; solid line indicates the power law fit.

slope up to the FIM ordering and a peaklike feature at lower temperatures. This suggests a possible magnetoelectric coupling nature near the critical value $x = 0.05$.

D. Magnetic, dielectric, and ferroelectric studies of Ni$_{0.95}$Zn$_{0.05}$Cr$_2$O$_4$

To obtain deeper insight into the magnetic and magneto-electric coupling of the Ni$_{0.95}$Zn$_{0.05}$Cr$_2$O$_4$ sample, a detailed magnetic and dielectric characterization was performed. The temperature-dependent ac susceptibility at the applied ac field of 1 Oe and different frequencies is displayed in Fig. 4(a). The ac susceptibility data exhibit a frequency-independent sharp peak at 41 K that confirms the long-range FIM ordering. By further decreasing the temperature, another broad frequency-independent peak is observed at 17 K, which suggests another long-range magnetic ordering. These transition temperatures are consistent with the T_{C1} and T_{C2} ZFC-FCC curves [Fig. 2(a)]. Between T_{C1} and T_{C2}, a smeared taillike feature is observed at 27 K, which coincides with the drop in ZFC magnetization. To further explore this feature, we performed ac susceptibility measurements with the application of a dc magnetic field at 3 kOe, which is displayed in Fig. 4(b). Under the dc magnetic field, a clear peak evolves from the taillike feature and becomes prominent with an increasing dc field [Fig. 4(c)]. This feature exhibits significant frequency dispersion, which is characteristic of several magnetic glass systems. However, T_{C1} and T_{C2} are slightly influenced by the dc magnetic field. The peak position shifts with frequency, and it was examined with the critical power-law variation. The plot of $\ln\tau$ vs T is shown in Fig. 4(d); the solid line indicates the fit to the power-law equation $\tau = \tau^* (\frac{T}{T_g} - 1)^{-zv}$, where zv, τ^*, and T_g denote the dynamic critical exponent, spin flip time, and glass transition temperature, respectively [28]. The solid line demonstrates satisfactory fitting of the experimental
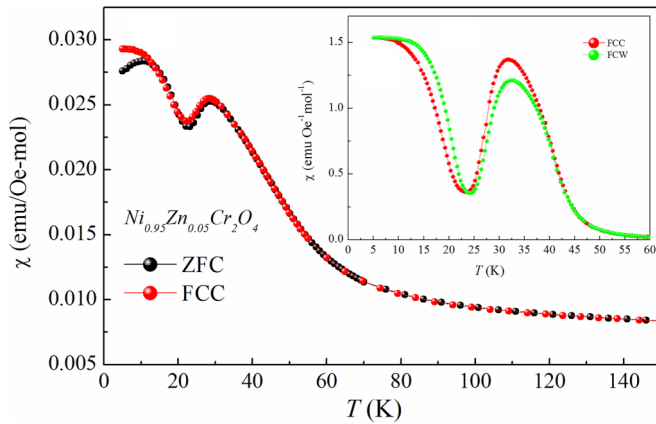
FIG. 5. ZFC-FCC magnetic susceptibility curves for an applied field of 5 T; inset shows the FCC and FCW magnetic susceptibility curves for an applied field of 100 Oe.

data, and the obtained fitting values are $zv = 5.33 \pm 0.69$, $\tau^* = (1.16 \pm 0.52) * 10^{-8}$ s, and $T_g = 25.41 \pm 2.3$ K. The observed fitting parameters are categorized as cluster glass behavior [29]. This complex magnetic behavior might be associated with a chemical-disorder-induced modulation of exchange couplings between Cr-Ni/Zn and Cr-Cr that helps to intensify the dynamical geometric frustration of the Cr sublattice [21]. Chemical disorder-induced short-range magnetic phases such as quasispin glass and reentrance spin glass have been reported in chromium spinels [6,30,31].

To reexamine the nature of this glassy magnetic transition, the magnetic susceptibility curves of $Ni_{0.95}Zn_{0.05}Cr_2O_4$ were plotted. The inset of Fig. 5 shows the FCC and field-cool warming (FCW) magnetic curves for the applied magnetic field of 100 Oe. Such a thermally driven magnetic hysteresis has been observed in several short-range magnetic phases, such as magnetic glassy, conical, or spiral magnetic ordering systems [29–31]. Furthermore, the merging of the ZFC-FCC curves for 5 T (Fig. 5) at T_{C1} and T_{C2} supports the hypothesis of long-range magnetic ordering.

The influence of the magnetic field on the dielectric property is shown in Fig. 6(a). Upon application of the 5 T magnetic field, the dielectric peak is suppressed below T_C. However, above T_C, the two curves merge, which confirms the existence of magnetoelectric coupling. The magnetic-field-dependent isothermal dielectric properties below and above T_C are shown in Fig. 6(b). Below T_C, the MD property shows a negative sign, in contrast to the positive MD behavior observed in $NiCr_2O_4$ [13]. Moreover, the MD property shows strong hysteresis between the field variations that is associated with the magnetic hysteresis below T_C [13]. However, the insensitive variation of the loss tangent with the field and the absence of the MD property above T_C demonstrate intrinsic MD behavior.

In general, dielectric anomalies in MF systems are associated with changes in the electric polarization, i.e., rotation or flip of the electric dipoles. Therefore, investigation of the ferroelectric property is necessary to understand MD behavior. For this purpose, the temperature dependence of the pyrocurrent was measured below T_C. As shown in the inset
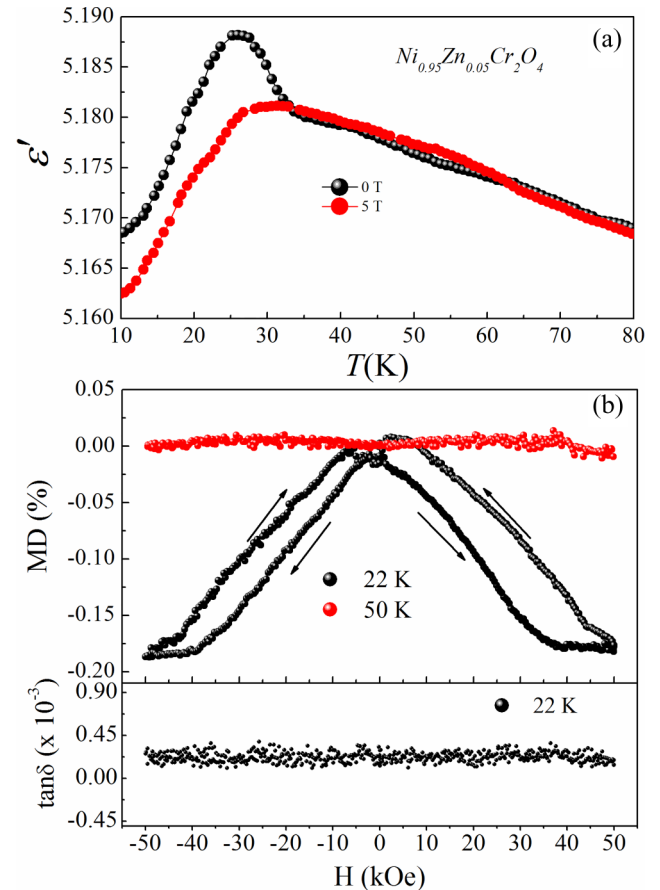

FIG. 6. (a) ε' vs T curves for 0 and 5 T. (b) Isothermal MD curves at 22 and 50 K; lower panel shows $\tan\delta$ vs H at 22 K.

of Fig. 7(a), the pyrocurrent exhibits weak but discernable peaks near the magnetic ordering temperatures, and the peak positions are invariant for several heating rates (not shown), which indicates true polarization. The polarization (P) was estimated by integrating the pyrocurrent with respect to time. The P shows distinct anomalies near T_{C1} and T_{C2} and a sign change of P with the application of a negative electric field; this suggests switchable polarization. The previously reported ferroelectric polarization of $NiCr_2O_4$ occurred above the magnetic ordering ($\sim$100 K), without anomalies near the magnetostructural transitions [32]. This indicates that the origin of P differs from that of $NiCr_2O_4$. Moreover, under the application of a 5 T field, a striking enhancement of P is observed between T_{C1} and T_{C2}. Furthermore, the observed P value of 0.7 $\mu C/m^2$ in $Ni_{0.95}Zn_{0.05}Cr_2O_4$ is smaller than that of most MF systems, suggesting that spin-canting-induced polarization might be the cause of the observed behavior. Reinvestigation of several well-known high P MF systems showed low intrinsic P values [33].

E. X-ray magnetic circular dichroism

It is well known that $ZnCr_2O_4$ shows SJT-induced AFM at 12 K. However, in $NiCr_2O_4$, FIM ordering develops because of the exchange interaction between the Ni-Cr ions [22]. Doping of Zn in the Ni site could change the local magnetic behavior of the Ni and Cr ions. Thus, XMCD is a valuable
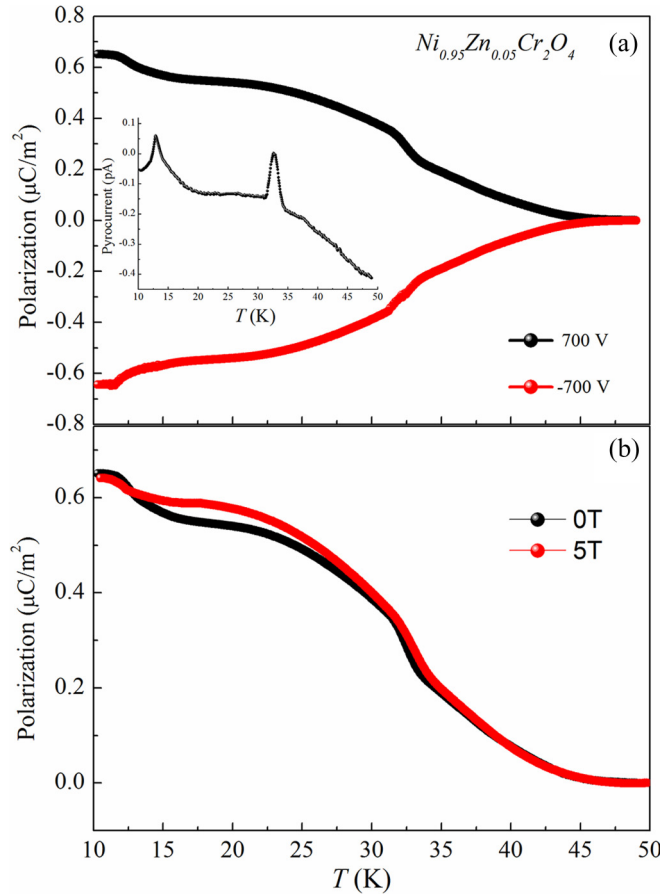
FIG. 7. (a) Polarization vs T curves for the applied electric field of $\pm 700\,\mathrm{V}$; inset shows the pyrocurrent vs T curve. (b) Polarization vs T curves for 0 and 5 T.

tool to investigate the magnetic behavior of specific elements and provides information of the orbital and spin magnetic moments. Based on certain selection rules, the orbital and spin magnetic moments of individual elements can be determined. We performed XMCD measurements of the Ni L edge. The XMCD data were collected in the FY mode with circularly polarized photons under a magnetic field of $\pm 1\,\mathrm{T}$ at 27 K. The XMCD signal was estimated by substrate of the x-ray absorption data for $+1$ and $-1\,\mathrm{T}$. As shown in Fig. 8(a), the XMCD signal for $NiCr_2O_4$ shows a peak and a dip at the L_{III} and L_{II} peaks, respectively. However, in the Zn-doped case, these features are progressively suppressed and disappear for the Zn concentration $x = 0.1$. This clearly indicates that the dilute doping of a non-JT ion at the JT site strongly influences the magnetic behavior of Ni. Moreover, the small XMCD signal of $Ni_{0.95}Zn_{0.05}Cr_2O_4$ indicates that the observed magnetic structure might not be a collinear configuration.

F. Low-temperature SXRD studies for $Ni_{0.95}Zn_{0.05}Cr_2O_4$

The observation of both complex magnetic behavior and dielectric anomalies might be intimately associated with structural transitions, as in the case of $NiCr_2O_4$. To confirm this, temperature-dependent SXRD measurements (300–12.5 K) were performed for the $Ni_{0.95}Zn_{0.05}Cr_2O_4$ sample. The two-
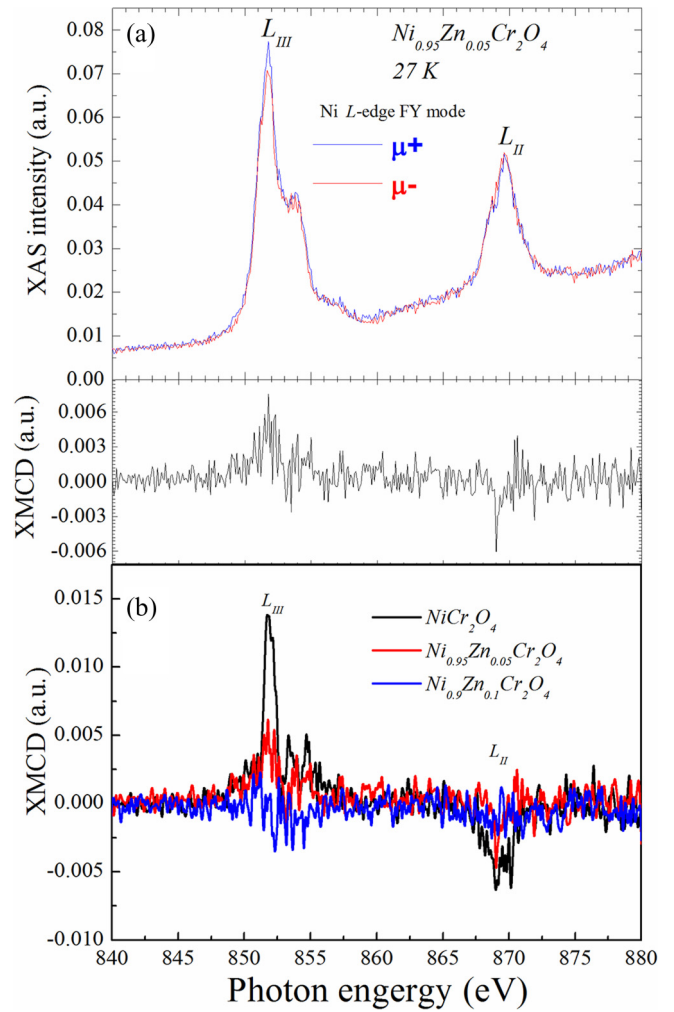

FIG. 8. (a) Typical x-ray absorption spectrum (XAS) and XMCD curves for $Ni_{0.95}Zn_{0.05}Cr_2O_4$ with an applied magnetic field of $B = 1\,\mathrm{T}$. (b) Comparison of the XMCD curves for $NiCr_2O_4$, $Ni_{0.95}Zn_{0.05}Cr_2O_4$, and $Ni_{0.9}Zn_{0.1}Cr_2O_4$.

dimensional (2D) project maps of the SXRD main reflection with temperature suggest crystal symmetry lowering from the cubic to the tetragonal phase (shown in Supplemental Material [25]), where the single cubic peak splits into two peaks ~200 K. This structural transition temperature is low compared to $NiCr_2O_4$, demonstrating that the minute chemical dilution at the Ni site strongly destabilizes the tetragonal phase. Below 200 K, the reflection in the SXRD patterns does not display significant change down to 12.5 K (shown in Supplemental Material [25]). This suggests that the dilution at the Ni site suppresses the orthorhombic phase transition that is observed in the parent $NiCr_2O_4$ sample.

To establish the temperature variation of the lattice parameters, a detailed structure analysis was performed using the Rietveld refinement method. The Rietveld fits of the SXRD patterns obtained at 300 and 12.5 K are shown in Fig. 9(a). At 300 K, the refinement fits the cubic crystal structure, whereas at 12.5 K, it leads to the tetragonal crystal structure. The evolution of the lattice parameters with temperature is shown in Fig. 9(b). The cubic-tetragonal phase transition was detected at 200 K.
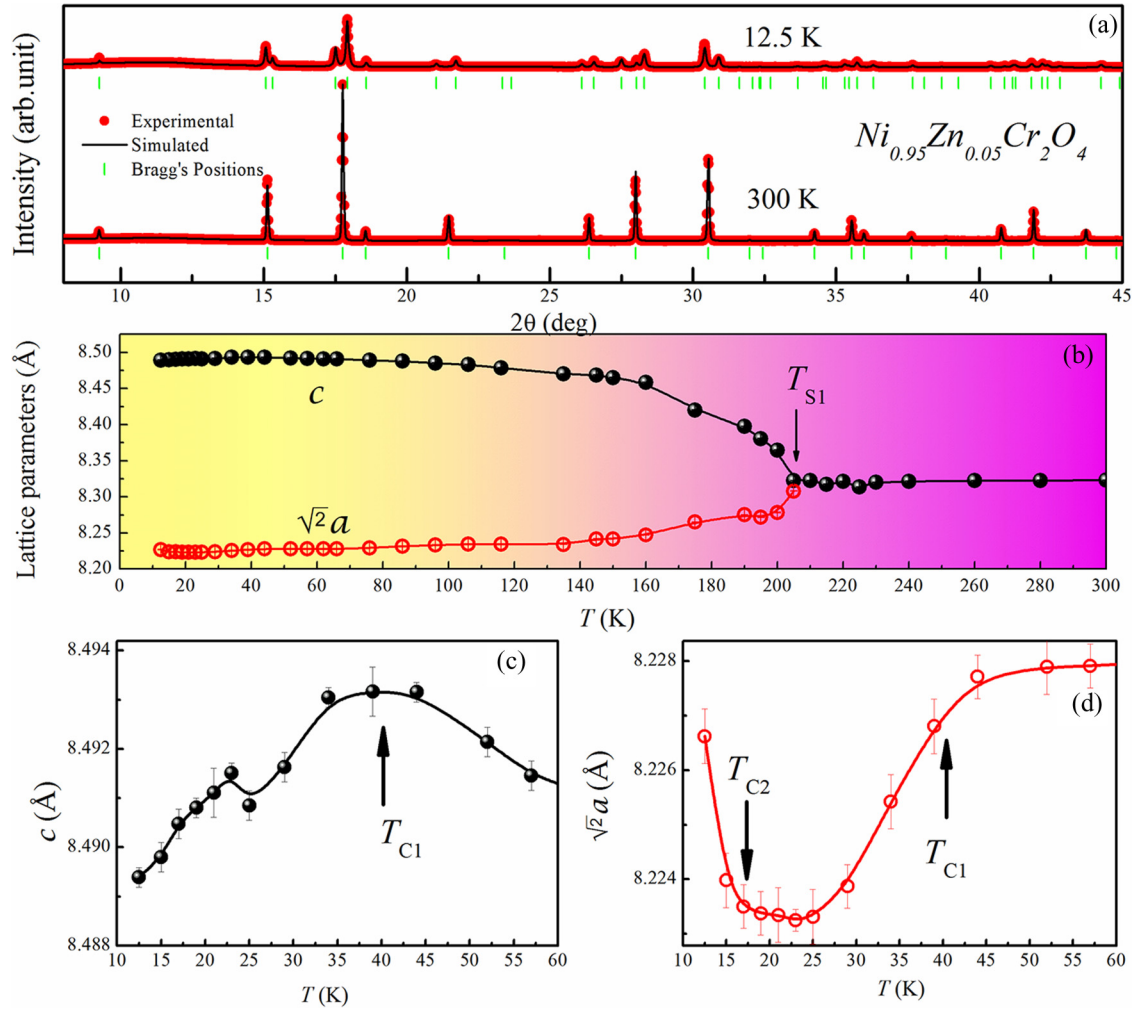
FIG. 9. (a) Rietveld refinement of $Ni_{0.95}Zn_{0.05}Cr_2O_4$ at 300 and 12.5 K. (b) Variation of the lattice parameter with respective to temperature. (c) and (d) Magnified view of lattice parameters below 60 K.

Furthermore, lowering of the temperature increases the tetragonal c axis but reduces the $\sqrt{2}a$-axis lattice parameter. A closer examination of the lattice parameters at low temperatures reveals obvious anomalies near T_{C1} and T_{C2} [Figs. 9(c) and 9(d)]. The tetragonal c axis shows a peaklike feature, whereas the a-axis lattice parameter displays a sharp decrease at the FIM transition. Although $Ni_{0.95}Zn_{0.05}Cr_2O_4$ does not exhibit a clear magnetostructural transition like $NiCr_2O_4$, the local structure shows some anomalies near the magnetic ordering temperatures that signify a considerable spin-lattice coupling in $Ni_{0.95}Zn_{0.05}Cr_2O_4$.

To further correlate the MD and ferroelectric properties with the crystal structure, the magnetization, MD, $\Delta P(P_{5T}-P_{0T})$, and pseudotetragonal lattice parameter ($\sqrt{2}a$) below 50 K are plotted in Fig. 10. The figure shows an obvious agreement between the structural and the property relations, where MD and ΔP are at their maximum between T_{C1} and T_{C2}. Outside the range $T_{C1}-T_{C2}$, MD and ΔP are essentially saturated. The one-to-one correspondence of the magnetization with MD and ΔP indicates that a magnetic structure between T_{C1} and T_{C2} is the cause of the MF property of $Ni_{0.95}Zn_{0.05}Cr_2O_4$. A detailed neutron diffraction analysis of $NiCr_2O_4$ has

determined two spin structure consisting of FIM and AFM components with propagation vectors $\mathbf{k}_1 = 0$ and $\mathbf{k}_2 = (0,0,1)$, respectively [22]. The propagation vector $\mathbf{k}_1$ corresponds to the FIM alignment of the Ni and Cr ions in the ab plane below 74 K, whereas $\mathbf{k}_2$ is connected with weak AFM coupling at the tetrahedral sites and the Cr moments point toward the c axis below 24 K [34]. In the present paper, the dilute doping of the non-JT Zn ion at a JT Ni site could strongly modulate the magnetic structure in the ab plane, which eliminates the magnetostructural transition of the parent $NiCr_2O_4$. However, in a tetragonal crystal, a structural relaxation of the $\sqrt{2}a$ lattice parameter has been observed near T_{C1} and T_{C2}. This indicates that the dilute doping of non-JT ion in the ab plane modulates the FIM exchange interactions that could lead to short-range ordering (such as spin spiral and conical) because of spin canting between T_{C1} and T_{C2}. Moreover, the observed low polarization values and the finite XMCD signal support that spin-canting-induced Dzyaloshinskii-Moriya magnetic interactions could be the source of the MF behavior in $Ni_{0.95}Zn_{0.05}Cr_2O_4$ [35]. Detailed neutron diffraction studies are in progress to verify this hypothesis.

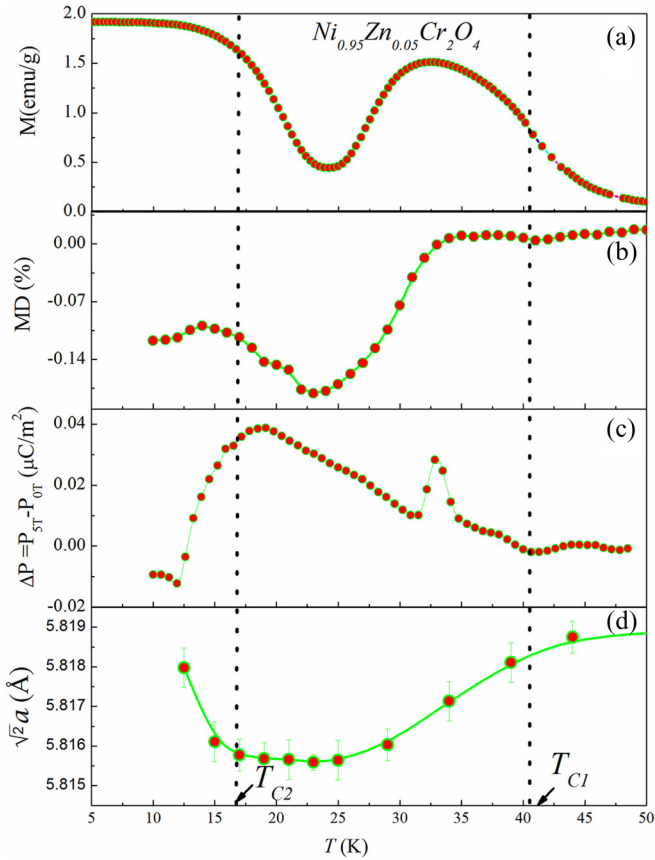FIG. 10. (a) M vs T, (b) MD percentage vs T, (c) ΔP vs T, and (d) $\sqrt{2}a$ vs T for $Ni_{0.95}Zn_{0.05}Cr_2O_4$.

IV. CONCLUSION

Polycrystalline $Ni_{1-x}Zn_xCr_2O_4$ samples were synthesized and a comprehensive MF study was performed using SXRD, magnetization, dielectric, XMCD, and MD measurements. A complex magnetic phase diagram was observed with respect to x. The magnetization measurements indicated the long-range magnetic ordering temperatures $T_{C1} = 41\,\mathrm{K}$ and $T_{C2} = 17\,\mathrm{K}$ for $x = 0.05$. Under a magnetic field, between T_{C1} and T_{C2}, short-range glasslike magnetic behavior developed because of the canting nature of the magnetic moments. The XMCD measurement at 27 K clearly indicated weak but uncompressed Ni magnetic moments for $x = 0.05$, which confirmed the spin-canting behavior. The temperature-dependent dielectric measurements indicated a change from the conventional dielectric to the quantum-paraelectric behavior for $x > 0.2$. The correlation among magnetization, dielectric, MD, and ferroelectric ordering with the structural relaxations indicates MF behavior for $x = 0.05$. The remarkable MF nature of $Ni_{0.95}Zn_{0.05}Cr_2O_4$ might originate from the Dzyaloshinskii-Moriya mechanism, in which the weak doping of non-JT ions modulates the different magnitudes of exchange strengths between Ni-Cr ions that might stabilize the spin-canting phenomena.

[1] S. H. Lee, C. Broholm, W. Ratcliff, G. Gasparovic, Q. Huang, T. H. Kim, and S. W. Cheong, Nature **418**, 856 (2002).

[2] V. Tsurkan, S. Zherlitsyn, S. Yasin, V. Felea, Y. Skourski, J. Deisenhofer, H.-A. K. von Nidda, J. Wosnitza, and A. Loidl, Phys. Rev. Lett. **110**, 115502 (2013).

[3] K. Aoyama and H. Kawamura, Phys. Rev. Lett. **116**, 257201 (2016).

[4] L. Balents, Nature **464**, 199 (2010).

[5] S. T. Bramwell and M. J. P. Gingras, Science **294**, 1495 (2001).

[6] A. D. LaForge, S. H. Pulido, R. J. Cava, B. C. Chan, and A. P. Ramirez, Phys. Rev. Lett. **110**, 017203 (2013).

[7] M. J. P. Gingras and P. A. McClarty, Rep. Prog. Phys. **77**, 056501 (2014).

[8] S. Bordács, D. Varjas, I. Kézsmárki, G. Mihály, L. Baldassarre, A. Abouelsayed, C. A. Kuntscher, K. Ohgushi, and Y. Tokura, Phys. Rev. Lett. **103**, 077205 (2009).

[9] S. Ji, S. H. Lee, C. Broholm, T. Y. Koo, W. Ratcliff, S. W. Cheong, and P. Zschack, Phys. Rev. Lett. **103**, 037201 (2009).

[10] V. Kocsis, S. Bordács, D. Varjas, K. Penc, A. Abouelsayed, C. A. Kuntscher, K. Ohgushi, Y. Tokura, and I. Kézsmárki, Phys. Rev. B **87**, 064416 (2013).

[11] Y. Yamasaki, S. Miyasaka, Y. Kaneko, J. P. He, T. Arima, and Y. Tokura, Phys. Rev. Lett. **96**, 207204 (2006).

[12] K. Singh, A. Maignan, C. Simon, and C. Martin, Appl. Phys. Lett. **99**, 172903 (2011).

[13] T. D. Sparks, M. C. Kemei, P. T. Barton, R. Seshadri, E.-D. Mun, and V. S. Zapf, Phys. Rev. B **89**, 024405 (2014).

[14] C. P. Sun, C. C. Lin, J. L. Her, C. J. Ho, S. Taran, H. Berger, B. K. Chaudhuri, and H. D. Yang, Phys. Rev. B **79**, 214116 (2009).

[15] C. P. Sun, C. L. Huang, C. C. Lin, J. L. Her, C. J. Ho, J.-Y. Lin, H. Berger, and H. D. Yang, Appl. Phys. Lett. **96**, 122109 (2010).

[16] M. C. Kemei, S. L. Moffitt, L. E. Darago, R. Seshadri, M. R. Suchomel, D. P. Shoemaker, K. Page, and J. Siewenie, Phys. Rev. B **89**, 174410 (2014).

[17] C. K. Moureen, T. B. Phillip, L. M. Stephanie, W. G. Michael, A. K. Joshua, S. Ram, R. S. Matthew, and K. Young-Il, J. Phys.: Condens. Matter **25**, 326001 (2013).

[18] J. S. Gardner, M. J. P. Gingras, and J. E. Greedan, Rev. Mod. Phys. **82**, 53 (2010).

[19] M. R. Suchomel, D. P. Shoemaker, L. Ribaud, M. C. Kemei, and R. Seshadri, Phys. Rev. B **86**, 054406 (2012).

[20] O. Crottaz, F. Kubel, and H. Schmid, J. Mater. Chem. **7**, 143 (1997).

[21] K. Tomiyasu, H. Hiraka, K. Ohoyama, and K. Yamada, J. Phys. Soc. Jpn. **77**, 124703 (2008).

[22] M. Reehuis, M. Tovar, D. M. Többens, P. Pattison, A. Hoser, and B. Lake, Phys. Rev. B **91**, 024407 (2015).

[23] G. D. Dwivedi, K. F. Tseng, C. L. Chan, P. Shahi, J. Lourembam, B. Chatterjee, A. K. Ghosh, H. D. Yang, and S. Chatterjee, Phys. Rev. B **82**, 134428 (2010).

[24] A. Kismarahardja, J. S. Brooks, H. D. Zhou, E. S. Choi, K. Matsubayashi, and Y. Uwatoko, Phys. Rev. B **87**, 054432 (2013).

[25] See Supplemental Material at http://link.aps.org/supplemental/10.1103/PhysRevB.94.205143 for a description of x-ray characterization.

[26] S. E. Dutton, Q. Huang, O. Tchernyshyov, C. L. Broholm, and R. J. Cava, Phys. Rev. B **83**, 064407 (2011).

[27] S. H. Lee, C. Broholm, T. H. Kim, W. Ratcliff, and S. W. Cheong, Phys. Rev. Lett. **84**, 3718 (2000).

[28] S.-P. Shen, Y.-S. Chai, J.-Z. Cong, P.-J. Sun, J. Lu, L.-Q. Yan, S.-G. Wang, and Y. Sun, Phys. Rev. B **90**, 180404 (2014).

[29] J. A. Mydosh, *Spin Glasses: An Experimental Introduction* (Taylor & Francis, London, UK, 1993).

[30] K. Tomiyasu, J. Fukunaga, and H. Suzuki, Phys. Rev. B **70**, 214434 (2004).

[31] A. Andreanov, J. T. Chalker, T. E. Saunders, and D. Sherrington, Phys. Rev. B **81**, 014406 (2010).

[32] A. Maignan, C. Martin, K. Singh, C. Simon, O. I. Lebedev, and S. Turner, J. Soli. Stat. Chem. **195**, 41 (2012).

[33] N. Terada, Y. S. Glazkova, and A. A. Belik, Phys. Rev. B **93**, 155127 (2016).

[34] K. Tomiyasu and I. Kagomiya, J. Phys. Soc. Jpn. **73**, 2539 (2004).

[35] C. Jia, S. Onoda, N. Nagaosa, and J. H. Han, Phys. Rev. B **76**, 144424 (2007).